Fermi surface interconnectivity and topology in Weyl fermion semimetals TaAs, TaP, NbAs, and NbP

Chi-Cheng Lee, Su-Yang Xu, Shin-Ming Huang, Daniel S. Sanchez, Ilya Belopolski, Guoqing Chang, Guang Bian, Nasser Alidoust, Hao Zheng, Madhab Neupane, Baokai Wang, Arun Bansil, M. Zahid Hasan, and Hsin Lin

Phys. Rev. B **92**, 235104 — Published 1 December 2015

DOI: 10.1103/PhysRevB.92.235104

Fermi surface interconnectivity and topology in Weyl fermion semimetals TaAs, TaP, NbAs, and NbP

Chi-Cheng Lee,[1,2] Su-Yang Xu,[3] Shin-Ming Huang,[1,2] Daniel S. Sanchez,[3] Ilya Belopolski,[3] Guoqing Chang,[1,2] Guang Bian,[3] Nasser Alidoust,[3] Hao Zheng,[3] Madhab Neupane,[3,4] Baokai Wang,[1,2,5] Arun Bansil,[5] M. Zahid Hasan,[3,6] and Hsin Lin[1,2]

[1]*Centre for Advanced 2D Materials and Graphene Research Centre National University of Singapore, 6 Science Drive 2, Singapore 117546*
[2]*Department of Physics, National University of Singapore, 2 Science Drive 3, Singapore 117542*
[3]*Laboratory for Topological Quantum Matter and Spectroscopy (B7), Department of Physics, Princeton University, Princeton, New Jersey 08544, USA*
[4]*Condensed Matter and Magnet Science Group, Los Alamos National Laboratory, Los Alamos, NM 87545, USA*
[5]*Department of Physics, Northeastern University, Boston, Massachusetts 02115, USA*
[6]*Princeton Center for Complex Materials, Princeton Institute for the Science and Technology of Materials, Princeton University, Princeton, New Jersey 08544, USA*

(Dated: October 22, 2015)

The family of binary compounds including TaAs, TaP, NbAs, and NbP was recently discovered as the first realization of Weyl semimetals. In order to develop a comprehensive description of the charge carriers in these Weyl semimetals, we performed a detailed and systematic electronic band structure calculations which reveal the nature of Fermi surfaces and their complex interconnectivity in TaAs, TaP, NbAs, and NbP. Our work report the first comparative and comprehensive study of Fermi surface topology and band structure details of all known members of the Weyl semimetal family, and hence provides the fundamental knowledge for realizing the many predicted exotic topological quantum physics of Weyl semimetals based on the TaAs class of materials.

I. INTRODUCTION

The discovery of Dirac fermions as low-energy quasi-particle excitations in graphene and on the surfaces of topological insulators has drawn significant attention in both fundamental physics research and device applications[1–34]. Since these Dirac-like fermions propagate as massless relativistic particles, they behave differently from the conventional charge carriers in metals, semiconductors, and insulators. Recently, a new form of massless fermions with lifted degeneracy at the nodal point, from four-fold to two-fold, has been proposed to exist in condensed matter systems through a time reserval or inversion symmetry breaking mechanism. This symmetry breaking operation modifies the quasi-particle's dispersion relation from a Dirac to a Weyl equation.[1–34] Many theoretical proposals exist for realizing Weyl semimetals that possess interesting physical properties, such as discontinuous Fermi arcs and negative magnetoresistance due to the chiral anomaly.[4,6–10,19–29,31,32,34] A Weyl node with definite chirality is associated with the Berry curvature and may be thought of as realizations of magnetic monopoles in momentum space.[30,61]

Recent theoretical works have proposed the realization of the Weyl semimetal state in the inversion symmetry breaking TaAs family.[11,13] Shortly after the prediction, the first Weyl semimetal was experimentally discovered in TaAs[12]. The electronic Weyl semimetal state in TaAs was experimentally observed through photoemission spectroscopy[12,14]. Electrical transport experiments have shown that TaAs has very high mobility[35] and, therefore, is consistent with the protected nature of the Weyl fermions and reported signatures of the chiral anomaly[36,37]. Soon after the initial experimental discovery other independent photoemission experimental works have confirmed the Weyl semimetal state in TaAs and, furthermore, the Weyl state in other members of the same family, which includes NbAs and TaP.[38–42]. This discovery paves the way for realizing the many predicted exotic topological quantum phenomena of Weyl semimetals in the TaAs class of materials[9,25–34]. For any ongoing[35–37,42–51] or future experiments on these materials, systematic knowledge of the band structure and Fermi surface is crucial and fundamental in understanding and interpreting their data and observations. However, surprisingly, a comprehensive study of the band structure details of the TaAs Weyl semimetal family has been lacking. Here, we report the first comparative and comprehensive study of Fermi surface topology and band structure details of all known members of the Weyl semimetal family.

Previous theoretical studies of this family focused on establishing TaAs as a Weyl semimetal and therefore only reported a few key aspects of the electronic structure for that purpose. On the other hand, many systematic details of the band structure, which are crucial for spectroscopy and transport studies, have not been studied. Furthermore, a comparative study of the electronic structure of TaAs with the other members remains lacking. Here, we report the first comparative and comprehensive study of Fermi surface topology and band structure details of all known members of the Weyl semimetal family. Our work is crucial and fundamental for future investigations of the topological Weyl semimetal phase from the-

TABLE I. Experimental lattice parameters (cf. Fig. 1).

	TaAs	TaP	NbAs	NbP
a (Å)	3.437	3.318	3.452	3.334
c (Å)	11.656	11.363	11.679	11.376
u/c	0.333	0.334	0.333	0.334

oretical, experimental and application perspective based on the TaAs class of materials. The paper is organized in the following manner: In Section II we provide the computational details. In Section III, electronic band structures and density of states are studied to improve our basic understanding of these four compounds. In Section IV, we discuss the details of the Fermi velocities of Weyl fermions and Fermi surfaces. Finally, in Section V we present a brief discussion covering the important conclusions reached.

II. COMPUTATIONAL DETAIL

First-principles calculations of TaAs, TaP, NbAs, and NbP, which have space group $I4_1md$ (109), a body-centered-tetragonal structure, were performed using the OpenMX code. The OpenMX code was based on norm-conserving pseudopotentials generated with multi reference energies[52] and optimized pseudoatomic basis functions.[53,54] For each Ta atom, three, two, two, and one optimized radial functions were allocated for the s-, p-, d-, and f-orbitals ($s3p2d2f1$), respectively. For As, Nb, and P atoms, $s3p3d3f2$, $s3p3d3f1$, and $s3p3d2f1$ were adopted, respectively. A cut-off radius of 7 Bohr was adopted for Ta, Nb, and P basis functions while a 9 Bohr cut-off radius was used for the As basis functions. The spin-orbit coupling was taken into account through j-dependent pseudopotentials,[55] and the generalized gradient approximation (GGA) was adopted for the exchange-correlation energy functional.[56,57] The cut-off energy of 1000 Ry was used for numerical integrations and for the solution of the Poisson equation. For the quality of k-point sampling, a $17 \times 17 \times 5$ mesh for the conventional unit cell was adopted. The experimental lattice parameters were chosen in the calculations and are listed in Table I. The conventional unit cell and first Brillouin zone of the primitive unit cell of the representative TaAs is plotted in Fig. 1.

Throughout this paper, for brevity, we will label the crystal momentum in units of $(2\pi/a, 2\pi/a, 2\pi/c)$ unless otherwise specified.

III. ELECTRONIC STRUCTURE

In this section, the electronic band structure and density of states for the four Weyl semimetal compounds are presented. With the combination of Ta, or Nb, and As, or P, very similar electronic structures can be found and, therefore, illustrates a flexibility in realizing Weyl fermions among these four elements.

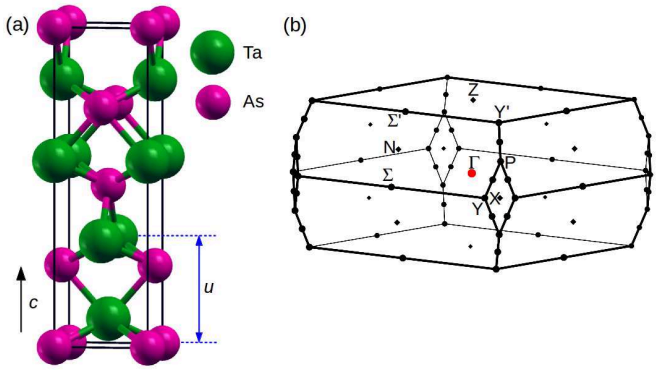

FIG. 1. (Color online). (a) Conventional unit cell of TaAs. (b) Primitive first Brillouin zone of TaAs. TaP, NbAs, and NbP share the same body-centered-tetragonal structure with different lattice parameters listed in Table I.

A. Symmetry

The relevant symmetry elements in the TaAs family (space group $I4_1md$) is the fourfold screw rotations along z-axis and two mirror reflections with respect to x- and y-axis. Due to lack of inversion symmetry, the rotation axis cannot sit perpendicular to the mirror planes. The combination of screw rotations and mirror reflections results in diagonal glide planes. Because the screw rotation and glide reflection are compound symmetry operations of translation and point group operations, for specific surface termination the surface states will not contain these compound symmetries. For the bulk, however, due to translation symmetry, the energy spectrum displays the C_4 and mirror symmetries. In k space, there are mirror planes at k_x=0, k_y=0 and $k_x \pm k_y$=0. The k_x=0 and k_y=0 mirror planes are important for the realization of Weyl nodes. On the mirror plane, each band can possess a mirror eigenvalue of either $+1$ or -1 ($+i$ or $-i$) in the absence (presence) of spin-orbit coupling, respectively. Bands with opposite mirror eigenvalues are allowed to cross, and those with the same mirror eigenvalues are only permitted to anti-cross. The other symmetry is time-reversal, which is not a spatial symmetry. Since time-reversal symmetry relates $\vec{k}$ and $-\vec{k}$ states, its combination with the twofold rotation results in the energy spectrum being symmetric with respect to the $k_z = 0, 1$ planes.

Since a Weyl node is characterized by a chirality of ± 1, which is defined by the integration of Berry curvature, a pseudovector, over a closed k-space surface (in unit of 2π),[30,61], Weyl nodes related by mirror symmetry will possess an opposite chirality while those related by rotation and time-reversal symmetries will have the same chirality. Thus, a mirror pair of Weyl nodes, as

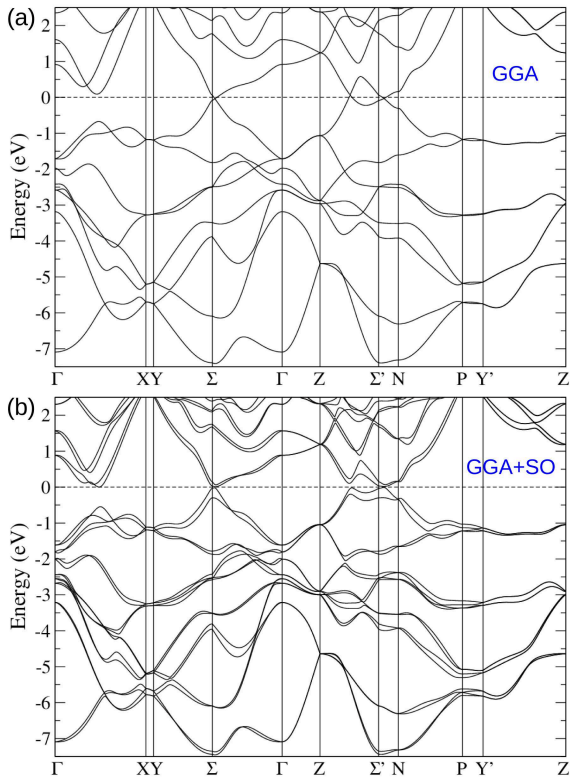

FIG. 2. Electronic band structure of TaAs (a) without and (b) with spin-orbit coupling.

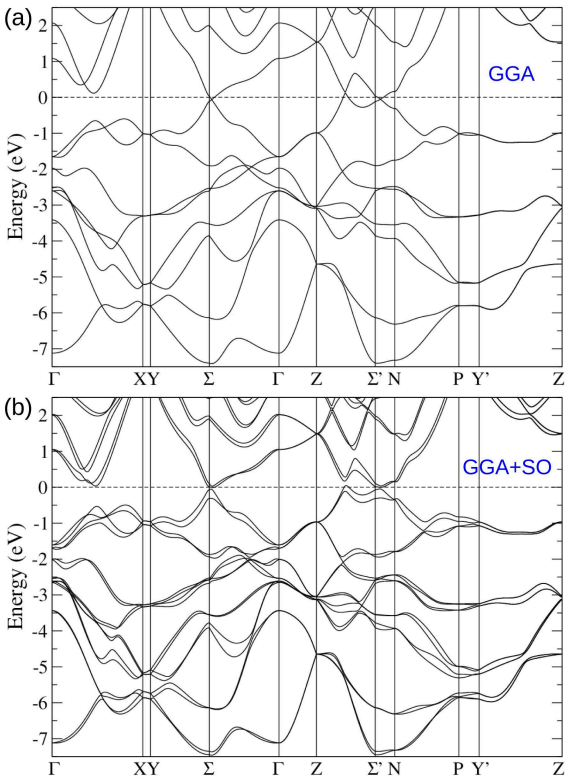

FIG. 3. Electronic band structure of TaP (a) without and (b) with spin-orbit coupling.

mirror images, will possess, relative to each other, an opposite chirality, and two Weyl nodes at equal k_x and k_y, but opposite k_z, will have the same chirality. Furthermore, the closed surface can be extended to a Fermi surface, yielding a Chern number for the Fermi surface[60] and, therefore, reflecting the net chirality of the enclosed Weyl nodes.

B. Band structure

The electronic band structures of TaAs, TaP, NbAs, and NbP with and without spin-orbit coupling are shown in Figs. 2, 3, 4, and 5, respectively. As expected, the band structures of these four Weyl semimetal compounds are characterized by the d orbitals of Ta or Nb atom, and the p orbitals of As or P atom are similar to one another near the Fermi energy. In the absence of spin-orbit coupling, the valence and conduction bands cross and form closed rings that are bounded on the mirror planes ($k_x = 0$ and $k_y = 0$ planes), due to the fact that both bands having opposite mirror eigenvalues. For the four Weyl semimetal compounds the nodal rings on the $k_x = 0$ mirror planes are shown in Fig. 6. Similarly, the location of nodal rings on the $k_y = 0$ mirror planes can be found by applying a C_4 rotation. Again, note that away from the mirror planes, which lack the necessary symmetry requirements,

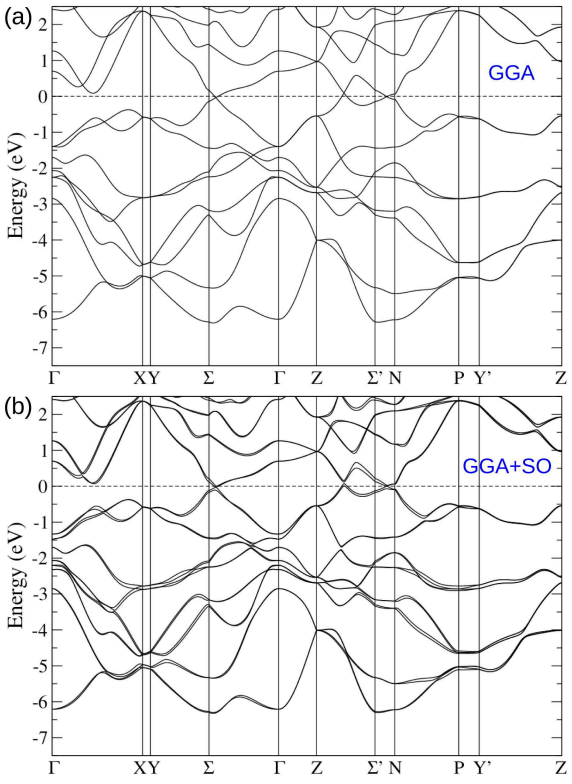

FIG. 4. Electronic band structure of NbAs (a) without and (b) with spin-orbit coupling.

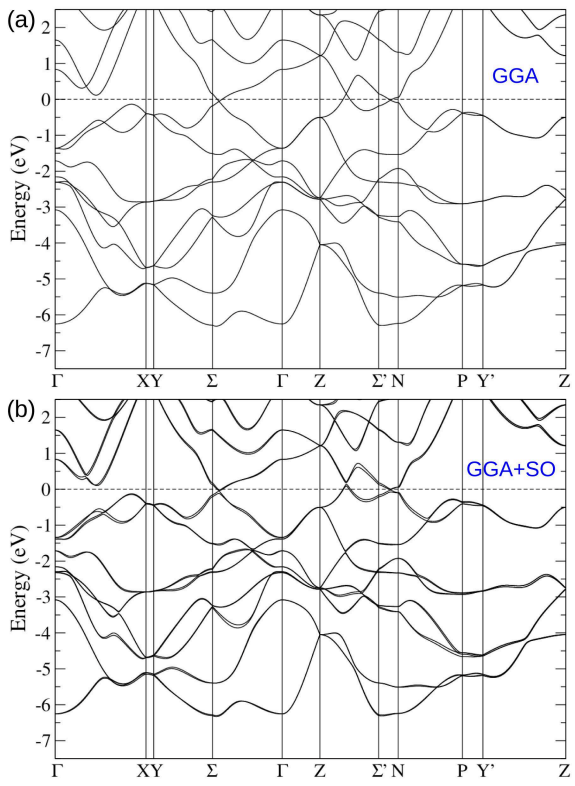

FIG. 5. Electronic band structure of NbP (a) without and (b) with spin-orbit coupling.

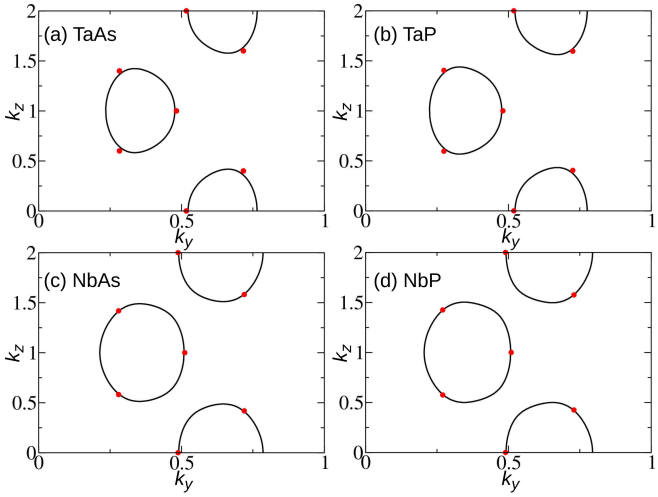

FIG. 6. (Color online). Line nodes on the k_x=0 plane formed by the crossing of valence and conduction bands in (a) TaAs, (b) TaP, (c) NbAs, and (d) NbP without spin-orbit coupling. The red solid circles indicated the projection of Weyl nodes on the k_x=0 plane after turning on the spin-orbit coupling. For each circle, two Weyl nodes of opposite chiralities on two sides of the k_x=0 plane are found.

accidental band crossings are not found.

In the presence of spin-orbit coupling, the aforementioned nodal rings no longer exist. The valence and conduction bands become fully gapped along the high symmetry lines, as shown in Figs. 2, 3, 4, and 5. The gap opening is smaller when replacing the Ta atom for an Nb atom, which indicates weaker spin-orbit coupling in NbAs and NbP and is consistent with the strong spin-orbit coupling in heavy elements.

The disappearance of nodal rings follows with the appearance of Weyl nodes. Pairs of Weyl nodes around the rings with opposite chirality on the two sides of the mirror planes are found.[11,13] For each ring in Fig. 6, three pairs of Weyl nodes are generated, and their locations, projected on the $k_x = 0$ plane, are indicated by the solid circles. The location of the other pairs of Weyl nodes can be obtained by applying a C_4 rotation, which uncovers 24 Weyl nodes for the first Brillouin zone. The detailed k-space coordinates and energies of two representative Weyl nodes are given in Table II. We denote Weyl nodes by W_1 for those at $k_z = n$ (multiples of $\frac{2\pi}{c}$), and by W_2 otherwise. The energies of W_1 are lower than those of W_2 for all of the studied compounds. For a Weyl node below (above) the Fermi energy, an electron (hole)- like Fermi surface will enclose a Weyl node, respectively.

Although the nodal rings are destroyed by spin-orbit coupling, new nodal rings are allowed to be created since the closest valence and conduction bands possess opposite mirror eigenvalues, $\pm i$. In other words, bands can cross on the plane with suitable hopping parameters. In NbAs, such a ring is found at $\vec{k} \approx$(0, 0.41, 1.47) with a tiny radius < 0.005. The negligible k -space area is in accordance with the energy overlap of only $\leq$0.2 meV for the ring. The energy of the ring is located approximately 5.4 meV above the Fermi energy. Since the energy overlap is tiny and occurs above the Fermi energy, we neglect the significance of this overlap in this study. The fact that spin-orbit coupling can annihilate or keep the nodal lines indicates that these lines depend on the presence of mirror symmetry but are not protected by it. However, parity of the number of nodal lines is conserved because of topology.

TABLE II. The coordinates (in units of reciprocal lattice vectors of conventional unit cell) and energies (in units of eV) of two representative distinct Weyl nodes denoted as W_1 and W_2 are given below. In each compound the energy of W_2 is higher than that of W_1. $\pm$ stands for a mirror pair of Weyl nodes.

	coordinate of W_1	energy of W_1
TaAs	($\pm$0.0072, 0.4827, 1.0000)	-0.0221
TaP	($\pm$0.0074, 0.4809, 1.0000)	-0.0531
NbAs	($\pm$0.0025, 0.5116, 1.0000)	-0.0322
NbP	($\pm$0.0028, 0.5099, 1.0000)	-0.0534
	coordinate of W_2	energy of W_2
TaAs	($\pm$0.0185, 0.2831, 0.6000)	-0.0089
TaP	($\pm$0.0156, 0.2743, 0.5958)	0.0196
NbAs	($\pm$0.0062, 0.2800, 0.5816)	0.0042
NbP	($\pm$0.0049, 0.2703, 0.5750)	0.0259

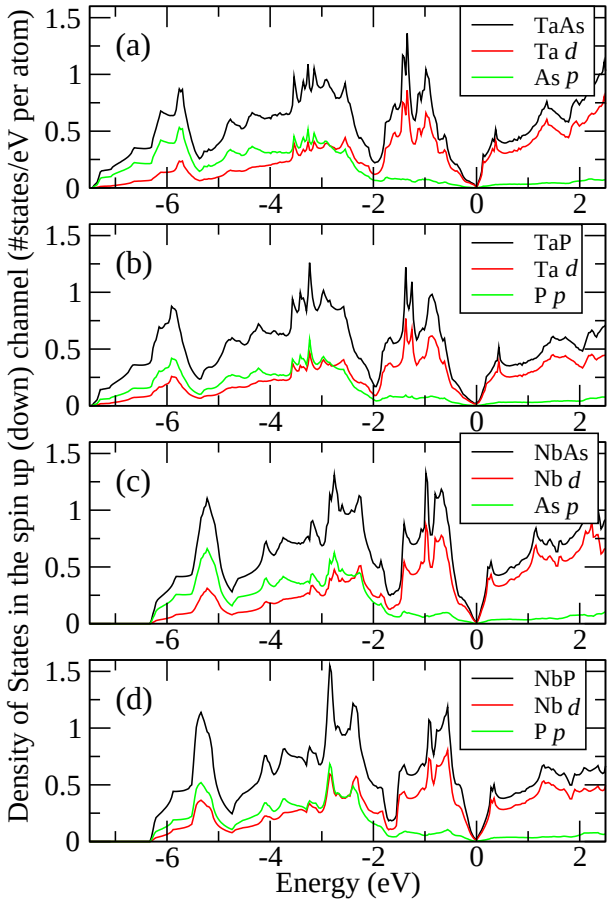

FIG. 7. (Color online). The orbital contributions of Ta d or Nb d and As p or P p in the density of states with spin-orbit coupling for (a) TaAs, (b) TaP, (c) NbAs, and (d) NbP are presented. The d and p contributions are colored red and green, respectively. The total formula contributions are plotted by black lines.

C. Density of states

TaAs, TaP, NbAs, and NbP have similar electron configurations in the outer shells, namely d^3s^2 and p^3 for Ta, or Nb, and As, or P, respectively. In order to fill the outer-most p orbitals of As and P, As^{3-}, P^{3-}, Ta^{3+}, and Nb^{3+} are expected according to the ionic-bonding picture, which should leave the Ta d or Nb d orbitals having a higher energy than the full-filled As p or P p orbitals. In Fig. 7, the partial density of states for Ta d, Nb d, As p, and P p are presented. One can directly observe that the d orbitals are strongly hybridized with the p orbitals. Although p character leads to the major contributions in the bottom band, the p orbitals are not fully occupied. In fact, the occupation numbers obtained in the basis of linear combination of atomic orbitals give only approximately half-filled p orbitals and the p orbitals also contribute to the energy above the Fermi energy. Therefore, it is inadequate to neglect the effect of p orbitals near the Fermi energy.

A simple picture to understand the obtained density of states is that of the Ta, or Nb, d orbitals hopping strongly to the As, or P, p orbitals and giving rise to the bonding and anti-bonding bands across the Fermi energy. The Ta, or Nb, s orbital also participates in the hybridization and does not donate itself completely. Having this hybridization scheme, the semimetal feature is formed, which shows the valence and conduction bands separated by a valley shaped density of states at the Fermi energy. The density of states are not zero at the Fermi energy due to the lack of particle-hole symmetry and the two distinct Weyl nodes (W_1, W_2) possessing different energies for each compound. Furthermore, the valence and conduction bands are found to cut through the Fermi energy and, therefore, forming hole and electron pockets, respectively. Note that the major contribution to the density of states around the Fermi energy is of d character. The bonding and anti-bonding p orbitals are split into much lower and higher energy.

Some additional information can be obtained from Fig. 7. TaAs and TaP share a wider bandwidth relative to the narrower bandwidth of NbAs and NbP, which reflects that $5d$ electrons are more delocalized than $4d$ electrons and that the replacement of As p by P p has less of an effect on the overall density of states. However, it is clearly observed that the density of states of P p in TaP is slightly lower than As p in TaAs. In addition, the density of states of P p in NbP is lower than As p in NbAs. This indicates that P p orbitals lose more electrons and are further away from the picture of fully-filled p orbitals. Another observation is that Nb d orbitals in NbP show the largest area below the Fermi energy and, therefore, possess the most d electrons out of the family of four Weyl semimetal compounds.

IV. CHARGE CARRIERS

In this section we investigate the properties of the Fermi surface. We first show the Fermi velocities of the Weyl fermions and the band dispersion between the energies of Weyl nodes and the Fermi energy for W_1 and W_2. Because of symmetry, we will show results for W_1 and W_2 at positive k_x, listed in Table II. Then the detailed studies of all the electron- and hole-like Fermi surfaces found in the four Weyl semimetal compounds are discussed.

A. Fermi velocity of Weyl fermion

In Weyl semimetals, the energies of Weyl nodes are close to the Fermi energy. Therefore, the physical properties of Weyl fermions are easy to experimentally access by slightly electron or hole doping the systems. The velocity of electron can be calculated by $(1/\hbar)dE/dk$. The details of how the slope of band dispersion varies between the W_1 or W_2 and the Fermi energy can be found in Fig. 8 and Fig. 9, respectively. The velocity at W_1 and

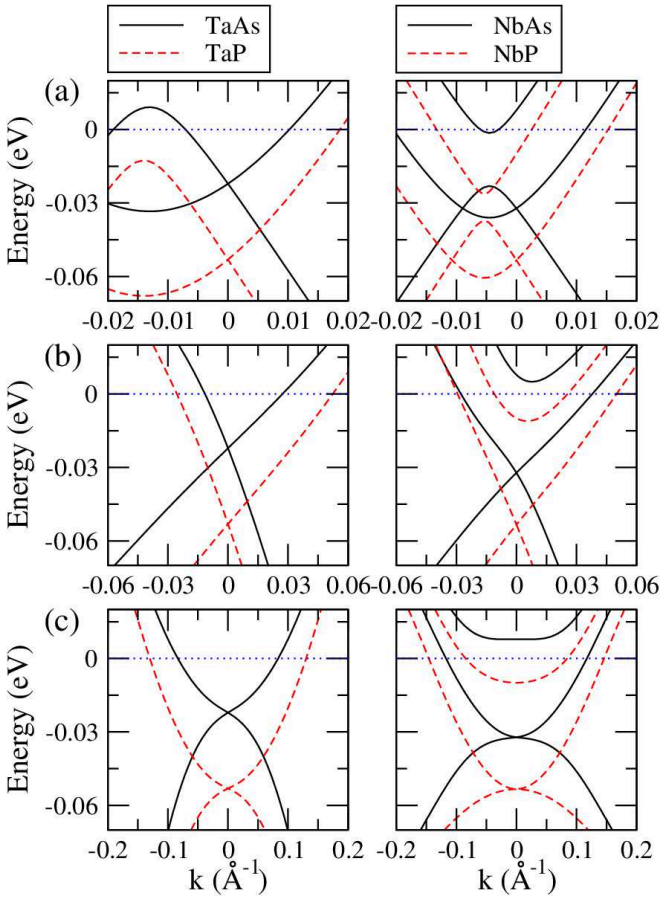

FIG. 8. (Color online). Band dispersion around W_1 along (a) k_x, (b) k_y, and (c) k_z directions of TaAs, TaP, NbAs, and NbP. The k-space coordinate of each Weyl node is set to 0.

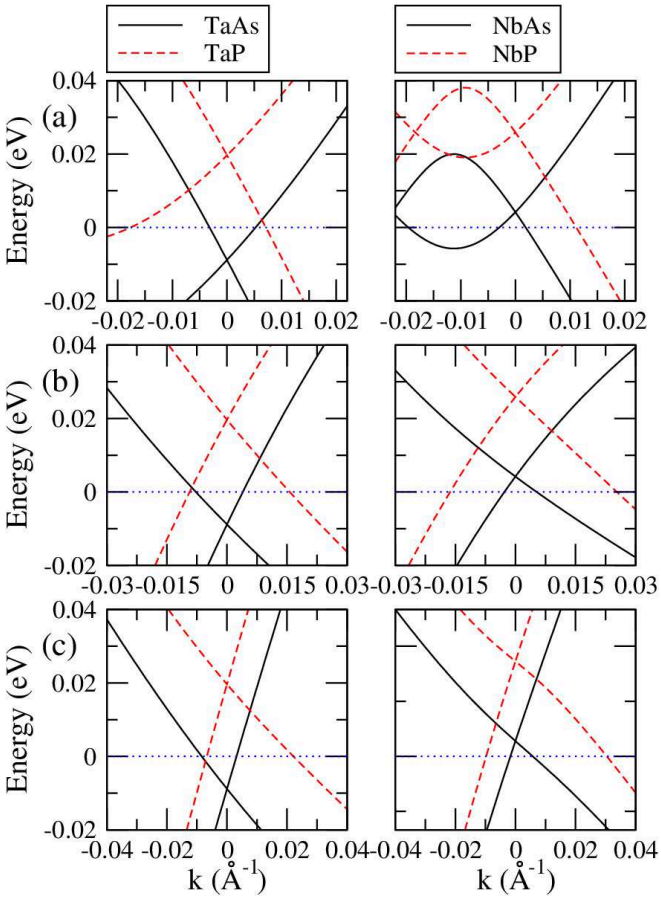

FIG. 9. (Color online). Band dispersion around W_2 along (a) k_x, (b) k_y, and (c) k_z directions of TaAs, TaP, NbAs, and NbP. The k-space coordinate of each Weyl node is set to 0.

W_2 along the k_x, k_y, and k_z directions are listed in Table III. As long as k is close enough to the Weyl nodes, the three-dimensional linear dispersive feature of Weyl cones is expected. It can be found that the velocities in Table III are highly anisotropic, and so are the band dispersions shown in Fig. 8 and Fig. 9. Consequently, the Fermi surface should exhibit such anisotropy. A detailed discussion of the Fermi surfaces will be addressed in the subsequent subsection.

TABLE III. Mean velocities at Weyl nodes along x, y, and z directions in units of 10^5 m·s^{-1}. c and v are for the conduction band and the valence band, respectively.

			TaAs	TaP	NbAs	NbP
W_1	v_x	c	2.5	3.1	2.5	3.7
	v_x	v	-5.2	-5.7	-4.8	-5.7
	v_y	c	1.2	1.5	1.2	1.5
	v_y	v	-3.2	-3.6	-2.0	-3.0
	v_z	c	0.2	0.2	0.1	0.0(3)
	v_z	v	-0.2	-0.2	-0.1	-0.0(3)
W_2	v_x	c	2.4	2.3	2.4	2.1
	v_x	v	-4.3	-4.1	-3.3	-3.2
	v_y	c	3.5	3.0	2.3	2.1
	v_y	v	-1.7	-2.0	-1.2	-1.6
	v_z	c	4.3	4.4	3.7	3.8
	v_z	v	-1.6	-1.5	-1.1	-1.0

B. Fermi surface

The properties of Fermi surfaces discussed below were calculated using discrete grids in k space. The calculations were performed using a conventional unit cell. Each length of the grid was 0.0015, 0.0015, and 0.005 reciprocal lattice vector along the k_x, k_y, and k_z direction, respectively. Information regarding the volume and cross-sectional area of Fermi surfaces and the Fermi velocities for each compound are listed in Tabel IV.

1. TaAs

The Fermi surfaces of TaAs are formed by both electron and hole pockets, which are shown in Fig. 10. According to Table II, both W_1 and W_2 are below the Fermi energy, with the latter being closer to it. As a result, an

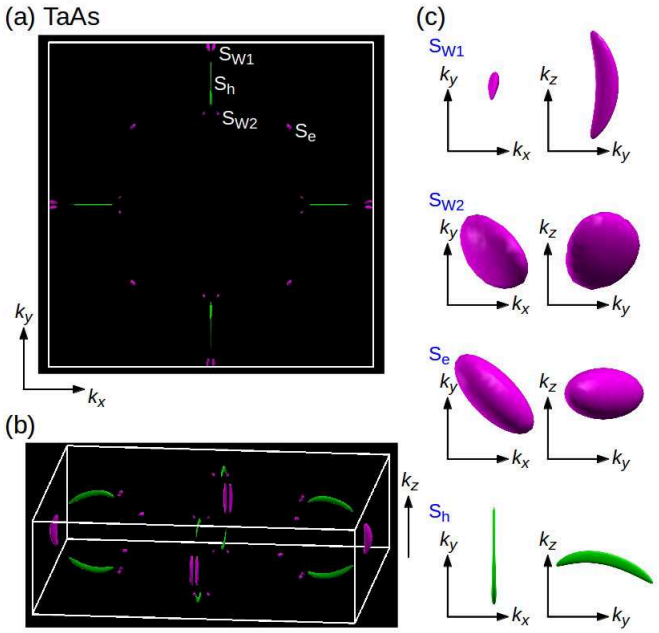

FIG. 10. (Color online). (a) Top view and (b) bird's eye view of TaAs Fermi surfaces in the first Brillouin zone of conventional unit cell with (c) the more detailed plots. Electron-like and hole-like Fermi surfaces are colored pink and green, respectively. S_{W1} (S_{W2}) is the Fermi surface enclosing the W_1 (W_2) Weyl node(s), and $S_e(S_h)$ is an electron (hole) pocket without enclosing any Weyl node.

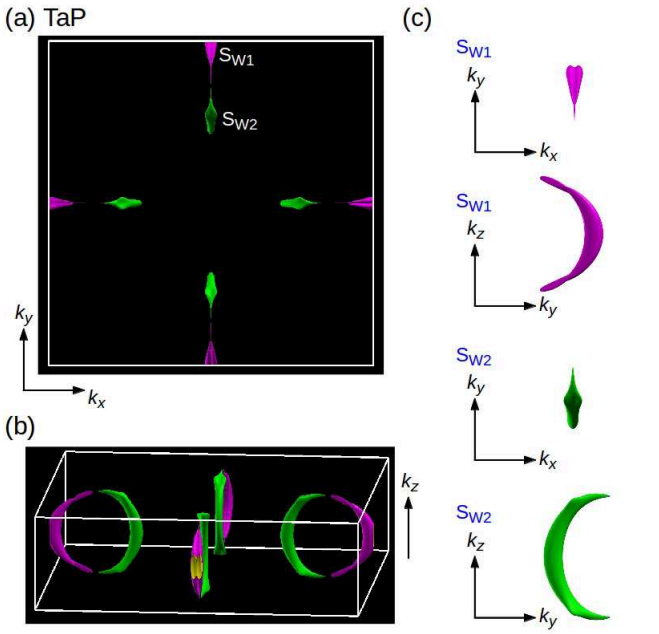

FIG. 11. (Color online). (a) Top view and (b) bird's eye view of TaP Fermi surfaces in the first Brillouin zone of conventional unit cell with (c) the more detailed plots. Electron-like and hole-like Fermi surfaces are colored pink and green, respectively. S_{W1} (S_{W2}) is the Fermi surface enclosing the W_1 (W_2) Weyl node(s).

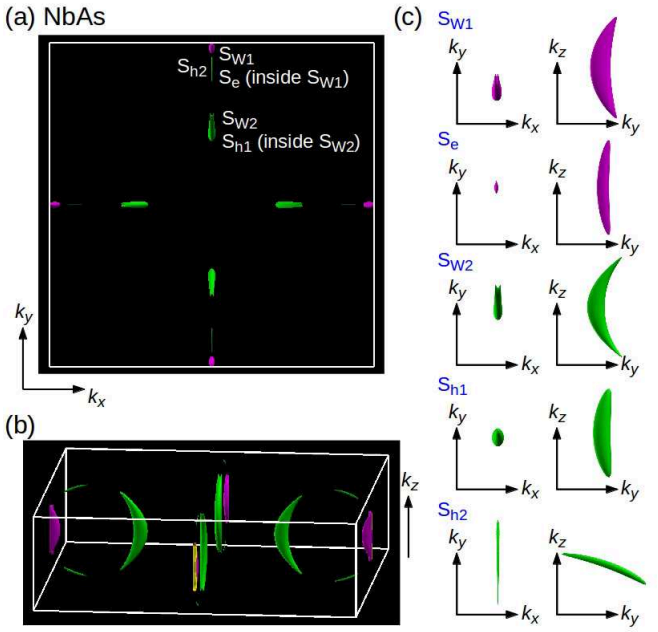

FIG. 12. (Color online). (a) Top view and (b) bird's eye view of NbAs Fermi surfaces in the first Brillouin zone of conventional unit cell with (c) the more detailed plots. Electron-like and hole-like Fermi surfaces are colored pink and green, respectively. S_{W1} (S_{W2}) is the Fermi surface enclosing and evolved from the W_1 (W_2) Weyl node(s), and $S_e(S_h)$ is an electron (hole) pocket not evolved from the Weyl node.

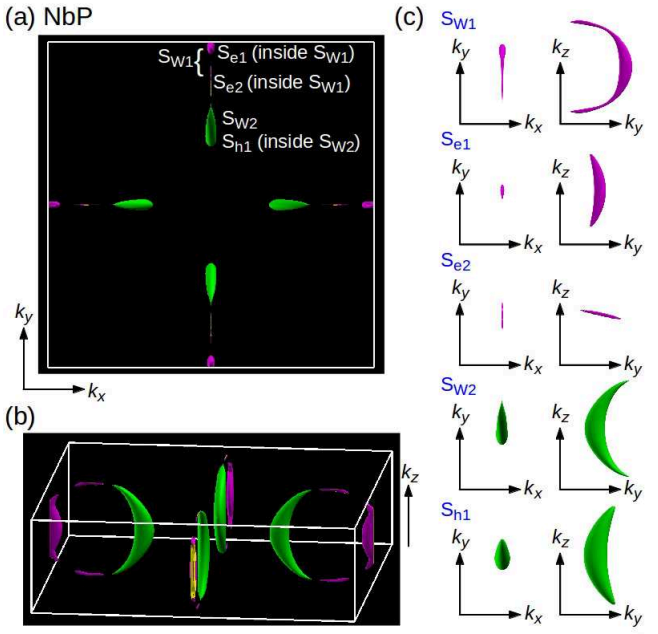

FIG. 13. (Color online). (a) Top view and (b) bird's eye view of NbP Fermi surfaces in the first Brillouin zone of conventional unit cell with (c) the more detailed plots. Electron-like and hole-like Fermi surfaces are colored pink and green, respectively. S_{W1} (S_{W2}) is the Fermi surface enclosing and evolved from the W_1 (W_2) Weyl node(s), and $S_e(S_h)$ is an electron (hole) pocket not evolved from the Weyl node.

electron pocket enclosing W_1 or W_2 Weyl node is expected. The Fermi surface of W_1 is much bigger than that of W_2 and shows high anisotropy along k_z. Some distance away from the end of the Fermi surface of W_1, a hole pocket centered on the mirror plane appears and extends to the neighborhood of the Fermi surface of W_2. Since each of the S_{W1} and S_{W2} Fermi surfaces encloses one Weyl node, the Fermi surface is endowed with a ± 1 Chern number.[60] Furthermore, the hole pocket does not surround any Weyl nodes, which is an outcome of the modulation of bands, and, consequently, carries a zero Chern number. The shape of the Fermi surfaces is reminiscent of the nodal rings in the absence of spin-orbit coupling. We note that different from the other compounds discussed below, the Fermi surfaces on two sides of a mirror plane are isolated instead of getting immersed, which is due to the distances between Weyl nodes and their energies relative to the Fermi energy. Furthermore, an electron pocket around (0.2425, 0.2425, 0) is found, which does not appear in other compounds. The details of the shapes and carrier concentrations can be found in Fig. 10 and Table IV. The maximal areas of the cross sections for the Fermi surfaces, which can be specifically measured by cyclotron experiments, are also listed in Table IV.

TABLE IV. Electron (e) and hole (h) carrier concentrations (n), maximal areas (A) of cross sections on the yz, xz, and xy planes, and root-mean-square velocities ($\bar{v}$) along the k_x, k_y, and k_z directions of Fermi surfaces ($cf.$ Fig. 10). $S_{W1}(S_{W2})$ is the Fermi surface enclosing and evolved from the $W_1(W_2)$ Weyl node(s), and $S_e(S_h)$ is an electron (hole) pocket Fermi surface not evolved from any Weyl node. The units of carrier concentration, area, and velocity are 10^{17} cm^{-3}, 10^{-3} Å^{-2}, and 10^5 m $\cdot$ s^{-1}, respectively.

TaAs		n	A_{yz}	A_{xz}	A_{xy}	$\bar{v}_x$	$\bar{v}_y$	$\bar{v}_z$
	$S_{W1}(e)$	3.336	6.060	2.557	0.639	2.920	1.532	0.453
	$S_{W2}(e)$	0.134	0.244	0.237	0.226	2.055	1.579	1.763
	S_e	0.364	0.406	0.406	0.624	0.365	0.365	0.412
	S_h	2.201	7.332	0.310	1.639	4.051	0.670	1.372
TaP		n	A_{yz}	A_{xz}	A_{xy}	$\bar{v}_x$	$\bar{v}_y$	$\bar{v}_z$
	$S_{W1}(e)$	48.98	23.67	15.87	4.687	3.270	1.594	0.767
	$S_{W2}(h)$	53.17	36.96	13.94	3.404	3.736	2.542	1.879
NbAs		n	A_{yz}	A_{xz}	A_{xy}	$\bar{v}_x$	$\bar{v}_y$	$\bar{v}_z$
	$S_{W1}(e)$	14.60	15.97	6.882	1.752	3.750	1.370	0.542
	$S_{W2}(h)$	29.76	24.57	10.29	2.646	4.647	2.647	1.765
	S_e	0.196	1.704	0.375	0.060	2.331	1.131	0.194
	S_{h1}	1.925	3.533	2.299	0.470	2.815	1.922	0.600
	S_{h2}	0.155	1.410	0.037	0.104	3.692	0.695	1.887
NbP		n	A_{yz}	A_{xz}	A_{xy}	$\bar{v}_x$	$\bar{v}_y$	$\bar{v}_z$
	$S_{W1}(e)$	32.64	31.47	10.78	2.805	4.047	1.653	0.932
	$S_{W2}(h)$	82.16	43.94	20.15	5.913	4.964	3.147	2.551
	S_{e1}	4.323	11.12	2.928	0.599	4.773	1.845	0.501
	S_{e2}	0.025	0.219	0.016	0.056	3.828	0.466	1.896
	S_{h1}	33.95	22.59	13.03	3.772	4.971	3.294	1.929

2. TaP

The Fermi surfaces of TaP are presented in Fig. 11. Contrary to TaAs, in which both energies of W_1 and W_2 are below the Fermi energy, the energy of W_1 and W_2 in TaP are below and above the Fermi energy, respectively shown in Table II. The W_2 in TaP is enclosed by a hole pocket Fermi surface. Due to higher energies of Weyl nodes away from the Fermi energy, the volume of Fermi surfaces are much larger (about $10 \sim 20$ times for S_{W1}) than those in TaAs. Furthermore, a Fermi surface encloses more than one Weyl node. An electron-like Fermi surface encompasses a mirror pair of W_1 points, while a hole-like Fermi surface covers two mirror pairs of W_2 points. Compared to that in TaAs, both electron and hole pockets take the shape of a crescents that are distributed more along the k_z direction. Except these electron and hole pockets there is no other piece of Fermi surfaces. The carrier concentrations and maximal areas of cross sections are listed in Table IV.

3. NbAs

The Fermi surfaces of NbAs are presented in Fig. 12. In NbAs, the energy of W_1 and W_2 are below and above the Fermi energy, respectively. Three types of hole-like Fermi surface are found in NbAs. The first kind encloses four W_2 points and passes through the $k_z = 0$ plane, like those found in TaP. The second kind is similar to those crescents elongated along the k_x or k_y, direction in TaAs. The third kind cannot be seen in Fig. 12 because the Fermi energy cuts through two spin split valence bands at $\vec{k} \approx (0, 0.2152, 0)$. Consequently, the inner surface is hidden inside the outer surface. In comparison with the W_1 points in TaAs and TaP, the two neighboring W_1 points are closer to each other. As a result, only one big crescent-shaped electron pocket containing two W_1 points is observed. Similar to the scenario of the two concentric-like hole pockets, there is also another electron pocket hidden inside the bigger Fermi surface near the W_1. The carrier concentrations and maximal areas of cross sections for each Fermi surface are listed in Table IV.

4. NbP

The Fermi surfaces of NbP are presented in Fig. 13. Similar to TaP and NbAs, the energy of W_1 and W_2 in NbAs are below and above the Fermi energy, respectively. The two concentric-like hole Fermi surfaces split by spin-orbit coupling are also present in NbP as intersecting the the k_z=0 plane at $\vec{k} \approx (0, 0.2042, 0)$, giving rise to four crescent Fermi surfaces in the first Brillouin zone with each surface containing one more surface inside. Each outer surface encloses one pair of W_2 points. In NbP, one long crescent electron-like Fermi surface resembling the shape of half a ring can be found. The surface be-

comes thinner while deviating from the W_1 and the detailed shape is easier to be observed in Fig. 13(c). There are two additional electron-like Fermi surface inside this long crescent surface, S_e1 and S_e2. Referring to the band dispersion in Fig. 8, we have to carefully identify the concentric electron pockets. Although S_e1 encloses one W1 point, the associated band does not evolve from the band of Weyl nodes and, therefore, is a trivial Fermi surface. The size of the surface S_e2 is small and touches the limit for the chosen grid size. The carrier concentration and maximal areas of cross sections for each Fermi surface is listed in Table IV.

V. DISCUSSION

Several interesting properties of the charge carriers can be found even without the consideration of additional conditions, like applying magnetic or strain fields in first-principles calculations. We first note that the energy difference between W_1 and W_2 is $\sim 10-100$ meV, which is realistic to access by doping in real crystals. The Fermi energy for TaAs was experimentally found[37] to be located between W_1 and W_2 (E_{W1} and E_{W2}, respectively), which is approximately 11.5 meV above E_{W1} and, therefore, different from our calculations shown in Table II.

The energy difference between two Weyl nodes is directly related to the minimal area of the Fermi surface as a function of binding energy, with a larger separation, $|E_{W2}-E_{W1}|$, corresponding to a larger minimal Fermi surface. Referring to Table II, the energy differences of E_{W2} and E_{W1} are 0.0132, 0.0727, 0.0364, and 0.0793 eV for TaAs, TaP, NbAs, and NbP, respectively. Recall, $E_{W2} > E_{W1}$. Note that while the separation in momentum space of the Weyl nodes is determined by the strength of the spin-orbit coupling, the separation in energy of the Weyl nodes can be viewed as arising from the dispersion of the spinless line node crossing, observed before spin-orbit coupling is introduced. Amongst the four Weyl semimetal compounds, the relatively small value for TaAs explains the relatively small carrier concentration, e.g. 0.134×10^{17} cm^{-3} for S_{W2}. Similarly, the largest hole pocket can be found in NbP, e.g. 82.16×10^{17} cm^{-3} for S_{W2}. The rich and tunable behavior of charge carriers in these four semimetals strongly suggests that these compounds are a good playground for engineering the electronic properties through doping, strain, electric fields, magnetic fields and/or other external perturbations.

Furthermore, we also point out that an abrupt change in the topology of the Fermi surface may occur by tuning the Fermi energy via, for example, doping, exhibiting a Lifshitz transition. Since each pair of Weyl nodes are located on two sides of the mirror plane, after turning on the spin-orbit coupling, they are, in general, close to each other. Therefore, there exists a critical Fermi energy that can make the two Fermi surfaces, each enclosing the Weyl node(s) on one side of the plane, touch at one k point. By changing the critical Fermi energy, either one big surface enclosing both Weyl nodes or two small surfaces with each enclosing a single Weyl node can be formed. The Fermi surfaces of the W_1 or W_2 pairs in TaAs is an example for the latter case while those in TaP, NbAs, and NbP are examples of the former case.

[1] Herman Weyl, Z. Phys. **56**, 330 (1929).

[2] Conyers Herring, Accidental Degeneracy in the Energy Bands of Crystals, *Physical Review* **52**, 365-373 (1937).

[3] A. A. Abrikosov, S. D. Beneslavskii, Some properties of gapless semiconductors of the second kind, *Journal of Low Temperature Physics* **5**, 141-154 (1971).

[4] Holger Bech Nielsen, Masao Ninomiya, The Adler-Bell-Jackiw anomaly and Weyl fermions in a crystal, *Physics Letters B*, **130**, 389-396 (1983).

[5] G. E. Volovik, *The Universe in a Helium Droplet* (Oxford University Press, 2009).

[6] Shuichi Murakami, Phase transition between the quantum spin Hall and insulator phases in 3D: emergence of a topological gapless phase, *New Journal of Physics*, **9** 356 (2007).

[7] Xiangang Wan, Ari M. Turner, Ashvin Vishwanath, Sergey Y. Savrasov, Topological semimetal and Fermi-arc surface states in the electronic structure of pyrochlore iridates, *Phys. Rev. B* **83**, 205101 (2011).

[8] Kai-Yu Yang, Yuan-Ming Lu, Ying Ran, Quantum Hall effects in a Weyl semimetal: Possible application in pyrochlore iridates, *Phys. Rev. B* **84**, 075129 (2011).

[9] Leon Balents, Viewpoint: Weyl electrons kiss, *Physics* **4**, 36 (2011).

[10] A. A. Burkov, Leon Balents, Weyl Semimetal in a Topological Insulator Multilayer, *Phys. Rev. Lett.* **107**, 127205 (2011).

[11] Shin-Ming Huang, Su-Yang Xu, Ilya Belopolski, Chi-Cheng Lee, Guoqing Chang, BaoKai Wang, Nasser Alidoust, Guang Bian, Madhab Neupane, Chenglong Zhang, Shuang Jia, Arun Bansil, Hsin Lin, M. Zahid Hasan, A Weyl Fermion semimetal with surface Fermi arcs in the transition metal monopnictide TaAs class, *Nature Communications* **6**, 7373 (2015).

[12] Su-Yang Xu, Ilya Belopolski, Nasser Alidoust, Madha Neupane, Guang Bian, Chenglong Zhang, Raman Sankar, Guoqing Chang, Zhujun Yuan, Chi-Cheng Lee, Shin-Ming Huang, Hao Zheng, Jie Ma, Daniel S. Sanchez, BaoKai Wang, Arun Bansil, Fangcheng Chou, Pavel P. Shibayev, Hsin Lin, Shuang Jia, M. Zahid Hasan, Discovery of a Weyl fermion semimetal and topological Fermi arcs, *Science* **349**, 613-617 (2015).

[13] Hongming Weng, Chen Fang, Zhong Fang, B. Andrei Bernevig, Xi Dai, Weyl Semimetal Phase in Noncentrosymmetric Transition-Metal Monophosphides, *Phys. Rev. X* **5**, 011029 (2015).

[14] B. Q. Lv, H. M. Weng, B. B. Fu, X. P. Wang, H. Miao, J. Ma, P. Richard, X. C. Huang, L. X. Zhao, G. F. Chen, Z.

Fang, X. Dai, T. Qian, H. Ding, Experimental Discovery of Weyl Semimetal TaAs, *Phys. Rev. X* **5**, 031013 (2015).

[15] A. H. Castro Neto, F. Guinea, N. M. R. Peres, K. S. Novoselov, A. K. Geim, The electronic properties of graphene, *Rev. Mod. Phys.* **81**, 109-162 (2009).

[16] S. Das Sarma, Shaffique Adam, E. H. Hwang,Enrico Rossi, Electronic transport in two-dimensional graphene, *Rev. Mod. Phys.* **83**, 407-470 (2011).

[17] M. Z. Hasan, C. L. Kane, *Colloquium* : Topological insulators, *Rev. Mod. Phys.* **82**, 3045-3067 (2010).

[18] Xiao-Liang Qi, Shou-Cheng Zhang, Topological insulators and superconductors, *Rev. Mod. Phys.* **83**, 1057-1110 (2011).

[19] F. D. M. Haldane, Attachment of Surface "Fermi Arcs" to the Bulk Fermi Surface: "Fermi-Level Plumbing" in Topological Metals. http://arxiv.org/abs/1401.0529 (2014).

[20] Bahadur Singh, Ashutosh Sharma, H. Lin, M. Z. Hasan, R. Prasad, A. Bansil, Topological electronic structure and Weyl semimetal in the $TlBiSe_2$ class of semiconductors, *Phys. Rev. B* **86**, 115208 (2012).

[21] A. M. Turner, A. Vishwanath, Beyond Band Insulators: Topology of Semi-metals and Interacting Phases. http://arxiv.org/abs/1301.0330 (2013).

[22] Gang Xu, Hongming Weng, Zhijun Wang, Xi Dai, Zhong Fang, Chern Semimetal and the Quantized Anomalous Hall Effect in $HgCr_2Se_4$, *Phys. Rev. Lett.* **107**, 186806 (2011).

[23] Daniel Bulmash, Chao-Xing Liu, Xiao-Liang Qi, Prediction of a Weyl semimetal in $Hg_{1-x-y}Cd_xMn_yTe$, *Phys. Rev. B* **89**, 081106 (2014).

[24] Jianpeng Liu, David Vanderbilt, Weyl semimetals from noncentrosymmetric topological insulators, *Phys. Rev. B* **90**, 155316 (2014).

[25] Pavan Hosur, S. A. Parameswaran, Ashvin Vishwanath, Charge Transport in Weyl Semimetals, *Phys. Rev. Lett.* **108**, 046602 (2012).

[26] Heon-Jung Kim, Ki-Seok Kim, J.-F. Wang, M. Sasaki, N. Satoh, A. Ohnishi, M. Kitaura, M. Yang, L. Li, Dirac versus Weyl Fermions in Topological Insulators: Adler-Bell-Jackiw Anomaly in Transport Phenomena, *Phys. Rev. Lett.* **111**, 246603 (2013).

[27] S. A. Parameswaran, T. Grover, D. A. Abanin, D. A. Pesin, A. Vishwanath, Probing the Chiral Anomaly with Nonlocal Transport in Three-Dimensional Topological Semimetals, *Phys. Rev. X* **4**, 031035 (2014).

[28] Pavan Hosur, Xiaoliang Qi, Recent developments in transport phenomena in Weyl semimetals, *Comptes Rendus Physique* **14**, 857-870 (2013).

[29] Andrew C Potter, Itamar Kimchi, Ashvin Vishwanath, Quantum oscillations from surface Fermi arcs in Weyl and Dirac semimetals, *Nature communications* **5**, 5161 (2014).

[30] Zhong Fang, Naoto Nagaosa, Kei S. Takahashi, Atsushi Asamitsu, Roland Mathieu, Takeshi Ogasawara, Hiroyuki Yamada, Masashi Kawasaki, Yoshinori Tokura, Kiyoyuki Terakura, The anomalous Hall effect and magnetic monopoles in momentum space, *Science* **302**, 92-95 (2003).

[31] Gábor B. Halász, Leon Balents, Time-reversal invariant realization of the Weyl semimetal phase, *Phys. Rev. B* **85**, 035103 (2012).

[32] A. A. Zyuzin, Si Wu, A. A. Burkov, Weyl semimetal with broken time reversal and inversion symmetries, *Phys. Rev. B* **85**, 165110 (2012).

[33] Tanmoy Das, Weyl semimetal and superconductor designed in an orbital-selective superlattice, *Phys. Rev. B* **88**, 035444 (2013).

[34] Teemu Ojanen, Helical Fermi arcs and surface states in time-reversal invariant Weyl semimetals, *Phys. Rev. B* **87**, 245112 (2013).

[35] C. Zhang, Z. Yuan, S. Xu, Z. Lin, B. Tong, M. Zahid Hasan, J. Wang, C. Zhang, S. Jia, Tantalum Monoarsenide: an Exotic Compensated Semimetal. http://arxiv.org/abs/1502.00251 (2015).

[36] X. Huang, L. Zhao, Y. Long, P. Wang, D. Chen, Z. Yang, H. Liang, M. Xue, H. Weng, Z. Fang, X. Dai, G. Chen, Observation of the chiral anomaly induced negative magneto-resistance in 3D Weyl semi-metal TaAs. http://arxiv.org/abs/1503.01304 (2015).

[37] C. Zhang, S.-Y. Xu, I. Belopolski, Z. Yuan, Z. Lin , B. Tong, N. Alidoust, C.-C. Lee, S.-M. Huang, H. Lin, M. Neupane, D. S. Sanchez, H. Zheng, G. Bian, J. Wang, C. Zhang, T. Neupert, M. Zahid Hasan, S. Jia, Observation of the Adler-Bell-Jackiw chiral anomaly in a Weyl semimetal. http://arxiv.org/abs/1503.02630 (2015).

[38] S.-Y. Xu, N. Alidoust, I. Belopolski, C. Zhang, G. Bian, T.-R. Chang, H. Zheng, V. Strokov, D. S. Sanchez, G. Chang, Z. Yuan, D. Mou, Y. Wu, L. Huang, C.-C. Lee, S.-M. Huang, B. Wang, A. Bansil, H.-T. Jeng, T. Neupert, A. Kaminski, H. Lin, S. Jia, and M. Zahid Hasan, Discovery of a Weyl fermion state with Fermi arcs in niobium arsenide. *Nature Physics* doi:10.1038/nphys3437 (2015).

[39] S.-Y. Xu, I. Belopolski, D. S. Sanchez, C. Guo, G. Chang, C. Zhang, G. Bian, Z. Yuan, H. Lu, Y. Feng, T.-R. Chang, P. P. Shibayev, M. L. Prokopovych, N. Alidoust, H. Zheng, C.-C. Lee, S.-M. Huang, R. Sankar, F. Chou, C.-H. Hsu, H.-T. Jeng, A. Bansil, T. Neupert, V. N. Strocov, H. Lin, S. Jia, M. Zahid Hasan, Experimental discovery of a topological Weyl semimetal state in TaP. http://arxiv.org/abs/1508.03102 (2015).

[40] B. Q. Lv, N. Xu, H. M. Weng, J. Z. Ma, P. Richard, X. C. Huang, L. X. Zhao, G. F. Chen, C. Matt, F. Bisti, V. Strokov, J. Mesot, Z. Fang, X. Dai, T. Qian, M. Shi, H. Ding, Observation of Weyl nodes in TaAs. *Nature Physics* doi:10.1038/nphys3426 (2015).

[41] N. Xu, H. M. Weng, B. Q. Lv, C. Matt, J. Park, F. Bisti, V. N. Strocov, D. Gawryluk, E. Pomjakushina, K. Conder, N. C. Plumb, M. Radovic, G. Autès, O. V. Yazyev, Z. Fang, X. Dai, G. Aeppli, T. Qian, J. Mesot, H. Ding, M. Shi, Observation of Weyl nodes and Fermi arcs in TaP. http://arxiv.org/abs/1507.03983 (2015).

[42] L. Yang, Z. Liu, Y, Sun, H. Peng, H. Yang, T. Zhang, B. Zhou, Y. Zhang, Y. Guo, M. Rahn , D. Prabhakaran, Z. Hussain , S.-K. Mo, C. Felser, B. Yan, Y. Chen, Discovery of a Weyl Semimetal in non-Centrosymmetric Compound TaAs, *Nature Physics* doi:10.1038/nphys3425 (2015).

[43] NJ Ghimire, Yongkang Luo, M Neupane, DJ Williams, ED Bauer, F Ronning, Magnetotransport of single crystalline NbAs, *Journal of Physics: Condensed Matter* **27**, 152201 (2015).

[44] Chandra Shekhar, Ajaya K. Nayak, Yan Sun, Marcus Schmidt, Michael Nicklas, Inge Leermakers, Uli Zeitler, Yurii Skourski, Jochen Wosnitza, Zhongkai Liu, Yulin Chen, Walter Schnelle, Horst Borrmann, Yuri Grin, Claudia Felser, Binghai Yan, Extremely large magnetoresistance and ultrahigh mobility in the topological Weyl semimetal candidate NbP, *Nature Physics* **11**, 645-649 (2015).

[45] Y. Luo, N. J. Ghimire, M. Wartenbe, M. Neupane, R.

D. McDonald, E. D. Bauer, J. D. Thompson, F. Ronning, A novel electron-hole compensation effect in NbAs. http://arxiv.org/abs/1506.01751 (2015).

[46] Z. Wang, Y. Zheng, Z. Shen, Y. Zhou, X. Yang, Y. Li, C. Feng, Z.-A. Xu, Helicity protected ultrahigh mobility Weyl fermions in NbP. http://arxiv.org/abs/1506.00924 (2015).

[47] C. Shekhar, F. Arnold, S.-C. Wu, Y. Sun, M. Schmidt, N. Kumar, A. G. Grushin, J. H. Bardarson, R. Donizeth dos Reis, M. Naumann, M. Baenitz, H. Borrmann, M. Nicklas, E. Hassinger, C. Felser, B. Yan, Large and unsaturated negative magnetoresistance induced by the chiral anomaly in the Weyl semimetal TaP. http://arxiv.org/abs/1506.06577 (2015).

[48] P. J. W. Moll, A. C. Potter, B. Ramshaw, K. Modic, S. Riggs, B. Zeng, N. J. Ghimire, E. D. Bauer, R. Kealhofer, N. Nair, F. Ronning, J. G. Analytis, Magnetic torque anomaly in the quantum limit of the Weyl semi-metal NbAs. http://arxiv.org/abs/1507.06981 (2015).

[49] Chenglong Zhang, Cheng Guo, Hong Lu, Xiao Zhang, Zhujun Yuan, Ziquan Lin, Junfeng Wang, and Shuang Jia, Large magnetoresistance over an extended temperature regime in monophosphides of tantalum and niobium, *Phys. Rev. B* **9**2, 041203 (2015).

[50] C. Zhang, Z. Lin, C. Guo, S.-Y. Xu, C.-C. Lee, H. Lu, S.-M. Huang, G. Chang, C.-H. Hsu, H. Lin, L. Li, C. Zhang, T. Neupert, M. Zahid Hasan, J. Wang, S. Jia, Quantum Phase Transitions in Weyl Semimetal Tantalum Monophosphide. http://arxiv.org/abs/1507.06301 (2015).

[51] J. Du, H. Wang, Q. Mao, R. Khan, B. Xu, Y. Zhou, Y. Zhang, J. Yang, B. Chen, C. Feng, M. Fang, Unsaturated both large positive and negative magnetoresistance in Weyl Semimetal TaP. http://arxiv.org/abs/1507.05246 (2015).

[52] I. Morrison and D.M. Bylander and L. Kleinman, *Phys. Rev. B* **"**47", 6728 (1993).

[53] T. Ozaki, *Phys. Rev. B*, **67**, 155108 (2003).

[54] T. Ozaki *et. al.*. http://www.openmx-square.org/.

[55] Gerhard Theurich,Nicola A. Hill, Self-consistent treatment of spin-orbit coupling in solids using relativistic fully separable *ab initio* pseudopotentials, *Phys. Rev. B* **64**, 073106 (2001).

[56] W. Kohn and L. J. Sham, *Phys. Rev.* **140**, A1133 (1965).

[57] J. P. Perdew and K. Burke and M. Ernzerhof, *Phys. Rev. Lett.* **77**, 3865 (1996).

[58] Jian-Hui Zhou and Hua Jiang and Qian Niu and Jun-Ren Shi, Topological invariants of metals and the related physical effects, *Chinese Physics Letters* **30**, 027101 (2013).

[59] Ching-Kai Chiu, Andreas P Schnyder, Classification of reflection-symmetry-protected topological semimetals and nodal superconductors, *Physical Review B* **90**, 205136 (2014).

[60] D. Gosalbez-Martinez, I. Souza, D. Vanderbilt, Chiral degeneracies and Fermi-surface Chern numbers in bcc Fe. http://arxiv.org/abs/1505.07727 (2015).

[61] Michael V Berry, Quantal phase factors accompanying adiabatic changes, *Proceedings of the Royal Society of London A: Mathematical, Physical and Engineering Sciences* **392**, 45-57 (1984).